energies

MDPI

Article

Performance Analysis and Modeling of a Tubular Staggered-Tooth Transverse-Flux PM Linear Machine

Shaohong Zhu, Ping Zheng *, Bin Yu, Luming Cheng and Weinan Wang

School of Electrical Engineering and Automation, Harbin Institute of Technology, Harbin 150080, Heilongjiang, China; auto_zsh@126.com (S.Z.); yubin1983@163.com (B.Y.); hitchengluming@126.com (L.C.); wangweinan19900501@163.com (W.W.)

* Correspondence: zhengping@hit.edu.cn; Tel./Fax: +86-451-8640-3086

Academic Editor: Enrico Sciubba

Received: 8 December 2015; Accepted: 22 February 2016; Published: 8 March 2016

Abstract: This paper investigates the performance analysis and mathematical modeling of a staggered-tooth transverse-flux permanent magnet linear synchronous machine (STTF-PMLSM), which is characterized by simple structure and low flux leakage. Firstly, the structure advantages and operation principle of the STTF-PMLSM are introduced, and a simplified one phase model is established to investigate the performance of the machine in order to save the computation time. Then, the electromagnetic characteristics, including no-load flux linkage, electromotive force (EMF), inductance, detent force and thrust force, are simulated and analyzed in detail. After that, the theoretical analysis of the detent force, thrust force, and power factor are carried out. And the theoretical analysis results are validated with 3-D finite-element method (FEM). Finally, an improved mathematical model of the machine based on *d*-*q* rotating coordinate system is proposed, in which inductance harmonics and coupling between *d*- and *q*-axis inductance is considered. The results from the proposed mathematical model are in accordance with the results from 3-D FEM, which proves the validity and effectiveness of the proposed mathematical model. This provides a powerful foundation for the control of the machine.

Keywords: transverse-flux permanent magnet linear machine; detent force; thrust force; 3-D finite-element method (FEM); mathematical model

1. Introduction

Linear drive systems integrated with linear electrical machines have many advantages, such as high dynamic performance, high acceleration, and easy maintenance compared with their rotary-to-linear counterparts [1]. Hence, linear machines are being used increasingly in applications ranging from manufacturing automation [2,3], electromagnetic launcher [4], transportation [5,6] and electrical power generation [7–9], to household appliances [10] and healthcare [11]. Within the various types of linear machines, tubular permanent magnet (PM) linear machines are quite promising for linear drive systems because of their distinctive features, including high power density, low force ripple, no unbalanced magnetic force on the shaft, and excellent servo characteristics, *etc.*

In recent years, the requirements for larger force density and higher position accuracy of linear machines are becoming increasingly urgent. For the traditional PM linear machine, the improvement of force density and power density are constrained by the space competition between the electric loading and magnetic loading. However, the transverse-flux PM linear machine is becoming particularly attractive for its larger force density because its motion direction is perpendicular to the plane of magnetic flux, which realizes the decoupling between electric loading and magnetic loading. The force density of the transverse-flux PM linear machine can be largely enhanced by decreasing the pole pitch or increasing the pole number of the machine for a given geometrical dimension [5]. Various

transverse-flux machine (TFM) topologies have been put forward since the first prototype of TFM with PM excitation was proposed by Weh in the 1980s [12–15]. A TFM with C-type stator core was proposed by the Rolls-Royce Research Center, in which the stator core is complex and it can only be made of soft magnetic composite (SMC), which will lead to low saturation magnetic flux density [13]. Chang has proposed a TFM with PM excitation for a direct drive system [16], but it also has the drawbacks of complex structure and large flux leakage. In 2014, Shin proposed two types of quadrate transverse-flux linear machine and research practical design approach for compact size, small mover weight, high efficiency, and low material cost [17,18]. Nevertheless, the problems of complex structure, large flux leakage, and difficult manufacturability always exist.

In order to solve the aforementioned problems, a novel tubular staggered-tooth transverse-flux permanent magnet linear synchronous machine (STTF-PMLSM) was proposed, which is characterized by simple structure and low flux leakage [19,20]. The stator core of the STTF-PMLSM is unsegmented and can be fabricated by silicon-iron steel lamination, which can largely simplify the manufacturing process and increase the mechanical strength. The 3-D magnetic equivalent circuit modeling and optimization of the machine was investigated, and an optimized scheme with higher force density and lower force ripple was achieved in [19].

The mathematical model of the machine is the foundation for the direct force control and vector control of the linear electrical machine. However, the conventional linear machine modeling methods cannot accurately describe the dynamic performance of the STTF-PMLSM due to its special inductance characteristics. Therefore, an improved mathematical model of the STTF-PMLSM based on a *d-q* rotating coordinate system is proposed, in which the inductance harmonics and coupling between *d*- and *q*-axis inductance are considered.

Hence, this paper focuses on the performance analysis and modeling of the STTF-PMLSM, which can be used for the control of the STTF-PMLSM. The structure advantages and operation principle of the STTF-PMLSM are introduced in Section 2. Then, the electromagnetic characteristics of the STTF-PMLSM, including winding inductance, detent force, thrust force, and power factor, are discussed in Section 3. In Section 4, an improved mathematical model of the STTF-PMLSM based on *d-q* rotating coordinate system is proposed and verified with 3-D finite-element method (FEM), which provides a powerful foundation for the control of the machine. Finally, some conclusions are summarized in Section 5.

2. Machine Structure and Operation Principle

2.1. Machine Structure

The overall schematic structure of the STTF-PMLSM is shown in Figure 1a, which is an axial 3-phase structure. The adjacent phases are arranged by (2*k*-2/3) pole pitch displacement in axial direction, where *k* is a non-negative integer (*k* = 2).

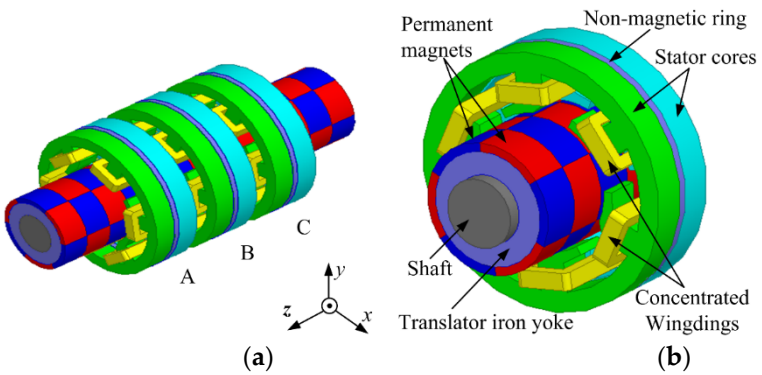

Figure 1. Schematic structure of STTF-PMLSM (**a**) Three phase; (**b**) One phase.

Figure 1b shows the schematic structure of one phase of the STTF-PMLSM. Each phase has j stator cores, where j is a non-negative integer (j = 2). Each stator core has $2n$ teeth, where n is a non-negative integer (n = 3). For every pole pair, primary side is constructed with two types of iron core and one non-magnetic ring, where the non-magnetic ring is used for fixation. The axial distance of adjacent stator cores of each phase is equal to one pole pitch. The concentrated winding of each phase is composed of $2n$ coils, which are wound around the roots of teeth and are connected in series. The surface-mounted PMs have tile shape and adjacent PMs are magnetized in opposite radial direction.

2.2. Operation Principle

The main magnetic flux paths in the two types of stator core are shown in Figure 2a,b which are perpendicular to the direction of motion, while the axial flux path exists in air gap, as shown in Figure 2c. Due to the staggered-tooth stator core, the PM fluxes in axially adjacent stator cores are in the same direction. This configuration functions as a bridge rectifier, which can force different magnetic flux path directions into the same direction. Moreover, the teeth of adjacent stator cores are staggered and have no overlap, which will greatly decrease the inter-pole flux leakage. Because the inter-pole flux leakage is the primary part of the total flux leakage, leakage reactance will reduce [19].

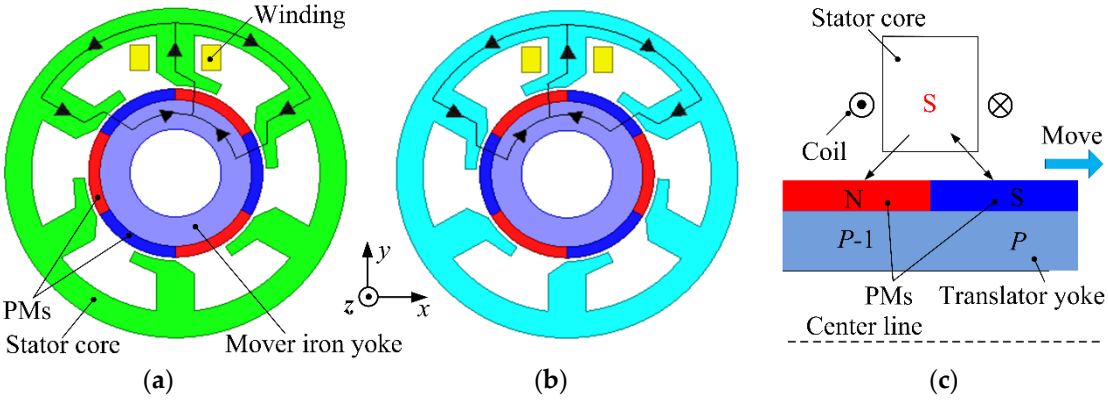

Figure 2. Magnetic flux path of STTF-PMLSM: (**a**) Main flux path in P-1 pole; (**b**) Main flux path in P pole; (**c**) Side view of the STTF-PMLSM.

The magnetic field of the STTF-PMLSM is not a traveling field such as a conventional linear PM machine but an alternating field to drive the motion of the translator. As shown in Figure 2c, when the armature winding is fed with a constant current, the south pole is generated at the salient pole in the stator core, then the translator will find a position where stator cores lie over the translator poles and the flux produced by the PM and by the winding will have the same direction. An inversion of excitation current will force the translator to move to the next pole. As a result, a longitudinal force is generated that drives the translator along z-direction when the armature winding is fed with an alternating current.

2.3. Structure Advantages

According to the aforementioned analysis, the structure advantages of the STTF-PMLSM can be summarized as follows:

(1) Simple structure. The structure of stator core is unsegmented and can be manufactured by silicon-iron steel lamination, which will result in a high mechanical stiffness and easy assembly.

(2) Easy manufacturability. The main magnetic flux paths of the STTF-PMLSM are in the plane of stator core lamination (x-y plane), which is transverse to the direction of movement (z-direction).

This configuration is preferable for the fabrication of stator core using silicon-iron steel laminations that are arranged along the *z*-direction.

(3) No unbalanced magnetic force on the supporting mechanism. The unbalanced magnetic force is eliminated by the balanced magnetic circuit of the symmetrical configuration of the stator core, which will greatly decrease the stress on the supporting mechanism and consequently improve the mechanical stiffness.

3. Analysis of Electromagnetic Characteristics

Compared with conventional linear electrical machine, the flux paths of the STTF-PMLSM are entirely 3-D distribution, including circumferential, radial and axial flux path, as shown in Figure 2. Moreover, the flux leakage of the STTF-PMLSM is more complicated. Therefore it's necessary to use 3-D FEM to analyze the electromagnetic characteristics of the STTF-PMLSM. Here, the commercial software package ANSYS Maxwell [21] is used since it can directly use the accurate finite element method to solve electromagnetic field and accurately predict product performance from physical design information with due account of saturation, leakage flux, *etc.* Due to the decoupling of the magnetic circuit of three phases, only one phase model is built in order to save the computation time. The main design specifications of the STTF-PMLSM are shown in Table 1 [19]. The flux distribution in the stator of the STTF-PMLSM under no-load conditions is shown in Figure 3.

Table 1. Main Design Specifications of STTF-PMLSM.

Parameters	Data	Parameters	Data
Stator outer radius (R_s)	90 mm	Number of phases	3
Stator inner radius (R_i)	48 mm	Number of stator slots	6
Air-gap length (g)	1 mm	Number of turns of the coil (N)	45
Pole pitch (τ)	9 mm	Rated current	8A
PM magnetization length (h_m)	3 mm	Rated frequency (f)	83.33 Hz
Axial length of stator core (l_s)	7 mm	Speed(v)	1 m/s
Material	Note	Material	Note
N35SH	PM (Br:1.23T)	DW315-50	Iron core

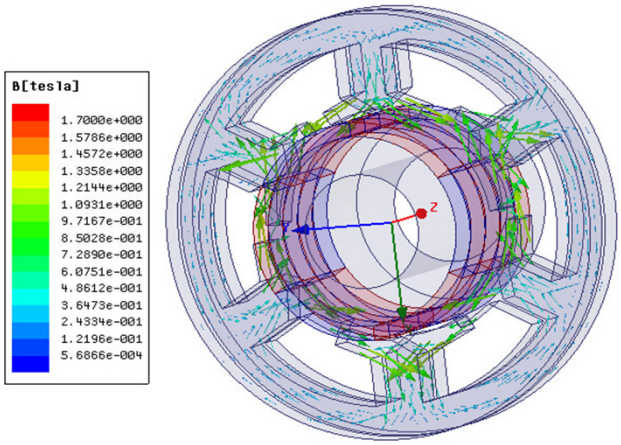

Figure 3. Flux distribution in the stator of STTF-PMLSM under no-load condition.

3.1. No-Load Main Flux Linkage

Figure 4a shows the waveforms of three phase no-load main flux linkage. Harmonics components of one phase flux linkage are show in Figure 4b. It can be seen that the waveform of flux linkage is close to sinusoidal and the amplitude of harmonics is very small. The total harmonic distortion (THD) is only 3.09%.

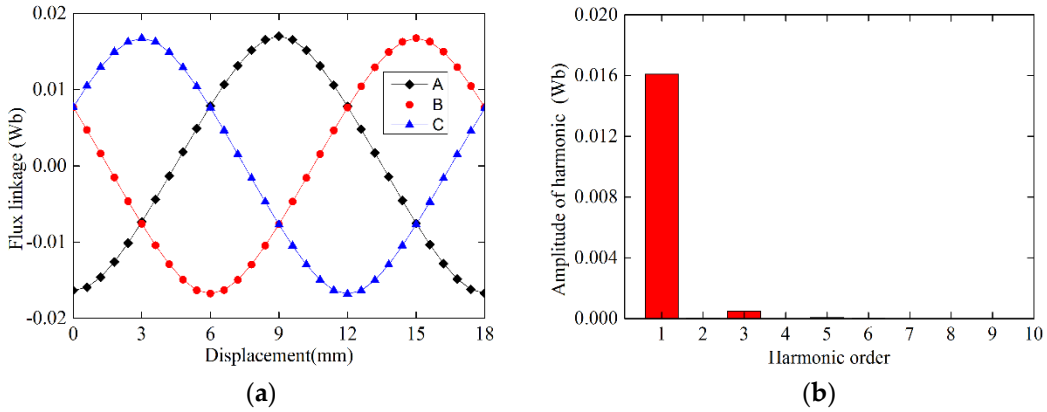

Figure 4. Flux linkage and its harmonics (**a**) Waveforms; (**b**) Harmonics components.

3.2. No-Load EMF

Figure 5a shows the waveforms of three phase no-load EMF. Harmonics components of one phase EMF are shown in Figure 5b. It should be noted that the shape of no-load EMF is somewhat close to trapezoidal. The third and fifth order harmonics are relatively large and the THD of EMF is 9.54%.

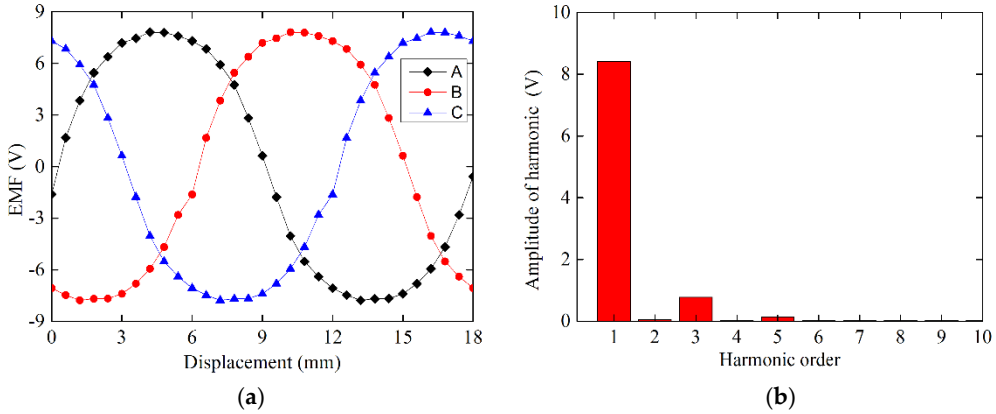

Figure 5. EMF and its harmonics (**a**) Waveforms; (**b**) Harmonics components.

3.3. Winding Inductance

In order to model the machine, it is necessary to calculate the winding inductance. Due to the decoupling of the three phases magnetic circuit, the mutual-inductance between different phases is equal to zero and can be neglected. Only the self-inductance is calculated. The self-inductance calculation method based on FEM is shown as:

$$L_{aa} = \frac{\psi_a - \psi_{a0}}{I_a} \tag{1}$$

where L_{aa} is self-inductance of phase A, ψ_a is flux linkage under load condition supply phase A with current I_a. ψ_{a0} is flux linkage under no-load condition.

Figure 6 shows the waveforms of three-phase self-inductance and its harmonics components. As we can see, the self-inductance is not constant. It contains some harmonics components and these harmonics are mainly the first, second and third order harmonic. These harmonics will result in the fluctuation of thrust force and this will be illustrated in Section 4.

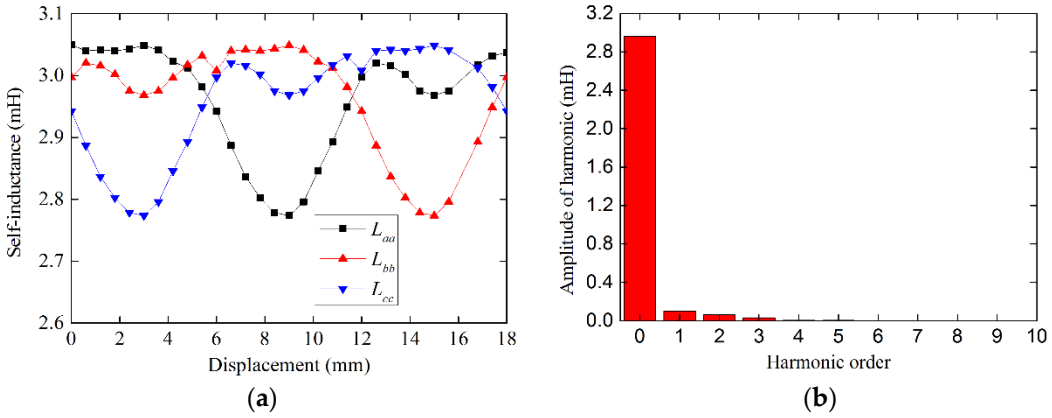

Figure 6. Self-inductances and its harmonic (**a**) Waveforms; (**b**) Harmonics components.

3.4. Detent Force

3.4.1. Theoretical Analysis of Detent Force

Detent force is a major problem in transverse flux linear machines, which will introduce thrust ripples or positioning process disturbances. The conventional methods like skewing and pole shifting used to reduce the detent force become impossible due to the special configuration of the STTF-PMLSM.

Detent force of the STTF-PMLSM is caused by two phenomena. The first one is called "end effect", which arises from the interaction between the translator and finite armature core length. The second one is called "slot effect", which arises from the interaction between PMs and armature slots [22]. The fundamental frequency of the detent force is the least common multiple (LCM) of the stator segment number and the pole number. For the STTF-PMLSM, the distance between two stator segments in the direction of the translator is τ, where τ is the pole pitch. When viewing the one-phase STTF-PMLSM from the direction of movement and the longitudinal end effect is neglected, the machine can be considered as a rotary machine with an infinite radius, $2N_1$ poles, and $2N_1$ stator segments, where N_1 is infinite. Therefore, the fundamental frequency of detent force for the one-phase STTF-PMLSM is $2N_1$, *i.e.*, the detent force period is τ [4].

The detent force of each phase can be decomposed into a Fourier series, which can be written as:

$$F_{da} = F_1\sin(\frac{z}{\tau}\times 2\pi+\theta_1)+F_2\sin2(\frac{z}{\tau}\times 2\pi+\theta_2)+F_3\sin3(\frac{z}{\tau}\times 2\pi+\theta_3)+\cdots\cdots \quad (2)$$

$$F_{db} = F_1\sin(\frac{z}{\tau}\times 2\pi+\theta_1-\frac{2}{3}\pi)+F_2\sin2(\frac{z}{\tau}\times 2\pi+\theta_2-\frac{2}{3}\pi)+F_3\sin3(\frac{z}{\tau}\times 2\pi+\theta_3-\frac{2}{3}\pi)+\cdots\cdots \quad (3)$$

$$F_{dc} = F_1\sin(\frac{z}{\tau}\times 2\pi+\theta_1+\frac{2}{3}\pi)+F_2\sin2(\frac{z}{\tau}\times 2\pi+\theta_2+\frac{2}{3}\pi)+F_3\sin3(\frac{z}{\tau}\times 2\pi+\theta_3+\frac{2}{3}\pi)+\cdots\cdots \quad (4)$$

where z is the displacement of translator, F_i is the amplitude of i order harmonic component (i = 1,2, ...). The total detent force (F_d) of the three-phase STTF-PMLSM can be expressed as:

$$F_d = F_{da}+F_{db}+F_{dc} = 3F_3\sin3(\frac{z}{\tau}\times 2\pi+\theta_3)+3F_6\sin6(\frac{z}{\tau}\times 2\pi+\theta_6)+\cdots\cdots \quad (5)$$

As can be seen from Equation (5), the period of the total detent force is $\tau/3$. Since the part of the harmonic components is counteracted, the amplitude of the total detent force is sharply reduced. Hence, the force ripple of the three-phase STTF-PMLSM is reduced.

3.4.2. Numerical Calculation of Detent Force

Figure 7 shows the waveforms of detent force computed by 3-D FEM, including three single phases and overall detent force of the STTF-PMLSM. As can be seen, the period of detent force of single

phase and total three phases are τ, $\tau/3$, respectively, which is in accordance with the aforementioned theoretical analysis. The error between total detent force directly calculated by FEM and the sum of three single phases detent force is nearly zero, and it can be neglected. This verifies the theoretical analysis of detent force.

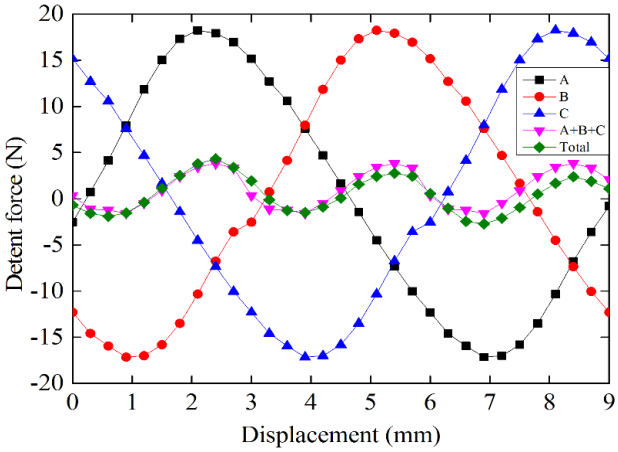

Figure 7. Detent force of STTF-PMLSM.

3.5. Thrust Force

3.5.1. Theoretical Analysis of Electromagnetic Force

When each phase is fed with a sinusoidal current, the electromagnetic force is produced by interaction between the armature and PM magnetic field. It can be calculated either by Maxwell stress tensor method or virtual work method. This paper choose latter one.

According to the magnetic co-energy theory, the electromagnetic force of the machine is equal to partial derivative of the total magnetic co-energy with respect to displacement [15], namely:

$$F = \frac{\partial W'(i,x)}{\partial x} \tag{6}$$

where $W'(i,x) = \int \psi di$, $\psi = \psi_{pm} + \psi_a$, $\psi_{pm} = 2Nn\Phi$, $\Phi = \Phi_m \cos(\theta)$. ψ_{pm} is the no-load total flux linkage interacting with the armature winding. Φ_m is the amplitude of no-load main flux. ψ_a is the flux linkage produced by armature current, and $\psi_a = Li$. L is the self-inductance of armature winding and i is the armature current. $i = -\sqrt{2}I\sin(wt + \theta_0)$, where I, θ_0 is the RMS and initial phase angle of armature current, respectively.

Therefore, the total magnetic co-energy can be expressed by:

$$W'(i,x) = \psi_{pm} i + \frac{1}{2} L i^2 \tag{7}$$

Since L is a constant independent on displacement, the third part of Equation (7) has no relation to the thrust force of translator. Considering $v = 2f\tau$ and $w = 2\pi f$, the electromagnetic force can be written as:

$$F = i\frac{\partial \Psi_{pm}}{\partial x} = -2\sqrt{2}NnjI\Phi_m \frac{\pi}{\tau}\sin\theta\sin(\theta + \theta_0) \tag{8}$$

where $\theta = wt$ is electrical angle corresponding to the displacement of translator.

If $i_d = 0$ control method is used, then $\theta_0 = 0^\circ$. Equation (8) can be simplified as:

$$F = \frac{2\sqrt{2}\pi}{\tau} NnjI\Phi_m \sin^2\left(\frac{x}{\tau} \times \pi\right) = F_o\left[1 - \cos\left(\frac{2x}{\tau} \times \pi\right)\right] \tag{9}$$

where $F_o = \frac{\sqrt{2}\pi}{\tau} NnjI\Phi_m$ is the average value of electromagnetic force of one phase STTF-PMLSM.

It can be observed that electromagnetic force of a one phase STTF-PMLSM is sinusoidal and its average value is greater than zero. The magnitude of the electromagnetic force of a one phase STTF-PMLSM is proportional to the number of coils, turns of each coil and no-load main flux. In addition, the period of electromagnetic force is τ, which means that electromagnetic force fluctuates twice in one period of alternating current. When each phase of the STTF-PMLSM is fed with the corresponding sinusoidal current, the per-phase electromagnetic force can be presented as:

$$F_a = F_o[1 - \cos(\frac{2x}{\tau} \times \pi)] \tag{10}$$

$$F_b = F_o[1 - \cos(\frac{2x}{\tau} \times \pi - \frac{2}{3}\pi)] \tag{11}$$

$$F_c = F_o[1 - \cos(\frac{2x}{\tau} \times \pi + \frac{2}{3}\pi)] \tag{12}$$

Hence, the total three-phase electromagnetic force of the STTF-PMLSM is as follows:

$$F = F_a + F_b + F_c = 3F_o \tag{13}$$

It can be seen that the total electromagnetic force of the STTF-PMLSM is constant and its magnitude is triple that of one phase. Hence, the feasibility of the approach that one phase of the STTF-PMLSM is chosen to investigate the performance of the machine is further confirmed.

Then, the force density of the three-phase STTF-PMLSM can be written as:

$$f = \frac{\sqrt{2}NnI\Phi_m}{R_s^2\tau^2} \tag{14}$$

It can be observed that the force density of the machine is inversely proportional to the pole pitch because ϕ_m in the numerator is proportional to the pole pitch τ and there is a τ^2 item in the denominator. This verifies the fact that a higher TFM force density can be obtained by increasing the pole number or decreasing the pole pitch of the machine for a given geometrical dimension [5].

3.5.2. Numerical Calculation of Electromagnetic Force

The force waveforms of one phase STTF-PMLSM computed by 3-D FEM, including electromagnetic force F_{ema}, detent force F_{dea} and thrust force F_a, are shown in Figure 8. It should be noted that the thrust force is obtained by subtracting the detent force from the electromagnetic force. The period of one phase thrust force is τ, and its shape is in accordance with the aforementioned theoretical analysis.

Figure 9 shows the waveforms of thrust force, including three single phases and overall thrust force of the STTF-PMLSM. As can be seen, the total thrust force is almost constant. The error between total thrust force directly calculated by 3-D FEM, and the sum of three single phases thrust force is nearly zero. It can further confirm that one phase of the STTF-PMLSM can be chose to investigate the performance of the machine. The average values of thrust force using different methods are summarized in Table 2. It can be observed that the results obtained from 3D-FEM are in accordance with theoretical analysis. In addition, the force density of the STTF-PMLSM is 2.822 $\times$ 10^5 N/m^3, which proves that the machine exhibits a higher force density compared with that of other types of linear machine, as illustrated in Section 3.7.

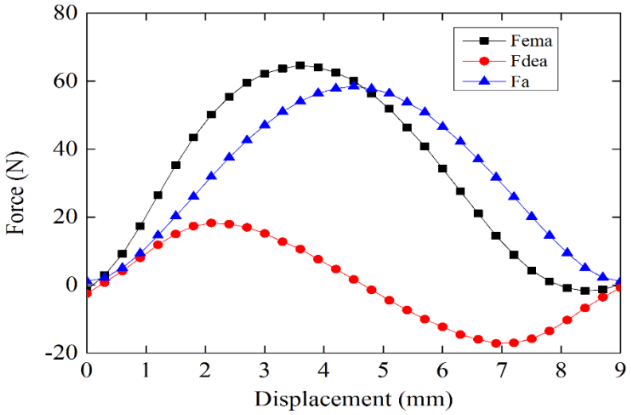

Figure 8. Force *versus* displacement of STTF-PMLSM.

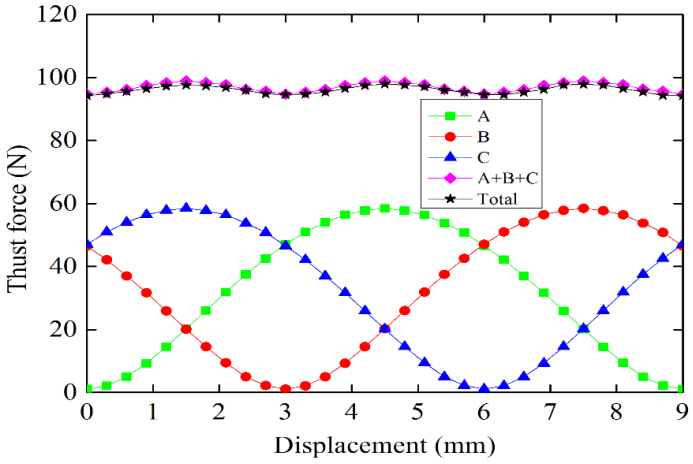

Figure 9. Thrust Force *versus* displacement of STTF-PMLSM.

Table 2. Thrust Force of STTF-PMLSM.

Thrust Force	from 3-D FEM	from Analysis	Error
F_o (one phase)	31.28	31.77	1.57%
F (three phase)	96.79	95.31	1.55%

3.6. Power Factor

The power factor of transverse-flux machine is relatively low, which is usually because the armature reactance and flux leakage of the machine are large. Furthermore, the power factor of the machine has a significant influence on the converter rating, which will increase the converter cost and converter loss. Therefore, it is necessary to analyze the power factor of the STTF-PMLSM. The inner power factor angle ψ_0 is the angle between the armature current and no-load EMF. When $i_d = 0$ control strategy is adopted ($\psi_0 = 0$), namely, the angle between current and no-load EMF is equal to zero. The phasor diagram of the machine is shown in Figure 10, where φ and θ are the power factor angle and torque angle, respectively. E_0 and E_δ are the no-load EMF and air-gap resultant EMF, respectively. L_1 and L_q are the stator leakage inductance and q-axis synchronous inductance, respectively. U, I_1 and R are the terminal voltage, armature current and stator resistance of each phase, respectively.

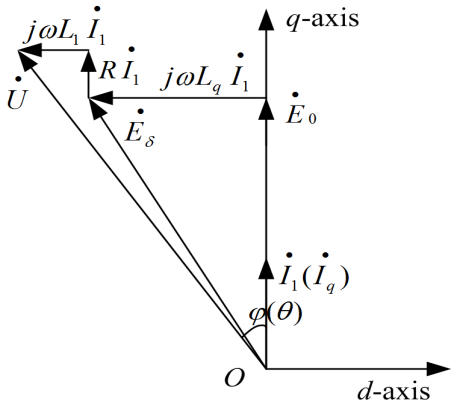

Figure 10. Phasor diagram of the machine under $i_d = 0$ control strategy.

Neglecting the stator leakage inductance and stator resistance, the expression of power factor [23] can be written as:

$$\cos\phi = \frac{E_0}{U} = \frac{E_0}{\sqrt{E_0^2 + (\omega L_q I_q)^2}} = \frac{1}{\sqrt{1 + (\frac{\omega L_q I_q}{E_0})^2}} \tag{15}$$

and this equation can also be expressed as:

$$\cos\phi = \cos(\arctan\frac{\omega L_q I_q}{E_0}) = \cos(\arctan\frac{\Phi_i}{\Phi_m}) \tag{16}$$

where ω is angular velocity, Φ_i is the amplitude of magnetic flux produced by the armature current alone:

It can be observed that a power factor improvement can be obtained by increasing the no-load EMF or decreasing the q-axis inductance from Equation (15). If the no-load EMF is constant, the power factor can also be enhanced when the armature current decreases from Equation (16), but this will lead to a reduction of force density or power density. The effective method to improve the power factor of the machine is to merely enhance the no-load main flux. However, this will increase the amount and cost of rare-earth PM material, which is not attractive for moving-magnet machines. Therefore, for all those methods, a compromise between high electromagnetic performance and cost should be made.

On the other hand, the power factor angle φ is equal to the phase angle difference between E_0 and E_δ from Figure 10 when the stator leakage inductance and stator resistance are negligible. The phase angle of the fundamental components of E_0 and E_δ can be directly calculated through the Fourier analysis, and the E_0 and E_δ can be calculated by 3-D FEM. Hence, the power factor can be directly calculated based on 3-D FEM results.

The power factor values based on theoretical analysis (mathematical expression) and 3-D FEM results are shown in Table 3. The error between the theoretical analysis and 3-D FEM is very tiny and this verifies the validity of the theoretical analysis. In addition, the power factor of the machine is relatively low, which is mainly caused by the large synchronous reactance. It should be noted that the value of L_d and L_q are 2.93 mH and 3.00 mH, respectively, which are obtained from Section 4.2.

Table 3. Power factor based on different methods.

Power Factor	from FEM	from Analysis	Error
value	0.440	0.433	1.62%

3.7. Performance Comparison

The performance comparison of various types of linear machines is shown in Table 4. It can be seen that force density (the thrust force per volume) of the STTF-PMLSM is lower than that of S type and TL-SPM, and higher than that of other types. On the other hand, the thrust force per air-gap area of the STTF-PMLSM is 37.06% higher than that of S type and it also the largest among these types. Furthermore, compared with other types, the thrust constant of the STTF-PMLSM is relatively low. Therefore, it is difficult to evaluate the superiority or inferiority of the STTF-PMLSM because of the different design conditions. However, it is confirmed that the STTF-PMLSM is close to the latest state of the art in linear machine technology [19].

Table 4. Performance comparison.

	STTF-PMLSM	**TL-IPM [2]**	**TL-SPM [4]**	**S type [2]**	**D type [2]**
Rated thrust (N)	96.79	79.4	125	800	2000
Rated current (A)	8	4	3	11.4	29.7
Thrust constant (N/A)	12.1	19.9	41.7	70.2	67.3
V_t (m^3)	3.43×10^{-4}	3.8×10^{-4}	4.6×10^{-4}	2.6×10^{-3}	8.7×10^{-3}
S_t (m^2)	3.99×10^{-3}	10.1×10^{-3}	–	45×10^{-3}	117×10^{-3}
F_{volume} (kN/m^3)	282.2	208.9	297	306.5	227.8
$F_{dimension}$ (kN/m^2)	24.26	7.86	–	17.7	17.1
Power factor	0.44	–	–	–	–

Abbreviations: TL-IPM: Tubular interior PM linear machine; TL-SPM: Tubular surface-mounted PM linear machine; S type: Single-sided type linear machine; D type: Double-sided type linear machine; F_{volume}: Thrust force per active external volume (V_t) [4]; $F_{dimension}$: Thrust force per active air-gap area(S_t) [4].

4. Mathematical Model of the STTF-PMLSM

4.1. Mathematical Model in Three-Phase Static Coordinate System

From Figure 4, the analytical expression of the three phase no-load flux linkage in the three-phase static coordinate system can be written as:

$$\begin{aligned} \psi_a &= -\psi_m \cos(\theta) \\ \psi_b &= -\psi_m \cos(\theta - 120^0) \\ \psi_c &= -\psi_m \cos(\theta + 120^0) \end{aligned} \tag{17}$$

where ψ_m is the fundamental amplitude of no-load flux linkage.

From the Fourier analysis results in Figure 6b, it can be seen that the main harmonic components of self-inductance are first-order, second-order and third-order harmonic. Besides, the mutual-inductances are zero. Hence, the analytical expression of the three phase self-inductances and mutual-inductances can be written as:

$$\begin{aligned} L_{aa} &= L_{DC} + L_{m1}\cos(\theta + \phi_1) + L_{m2}\cos 2(\theta + \phi_2) + L_{m3}\cos 3(\theta + \phi_3) \\ L_{bb} &= L_{DC} + L_{m1}\cos(\theta + \phi_1 - 120^0) + L_{m2}\cos 2(\theta + \phi_2 - 120^0) + L_{m3}\cos 3(\theta + \phi_3 - 120^0) \\ L_{cc} &= L_{DC} + L_{m1}\cos(\theta + \phi_1 + 120^0) + L_{m2}\cos 2(\theta + \phi_2 + 120^0) + L_{m3}\cos 3(\theta + \phi_3 + 120^0) \\ L_{ab} &= L_{ac} = L_{bc} = 0 \end{aligned} \tag{18}$$

where L_{DC} is the DC component of self-inductance, L_{mi} is the amplitude of i order harmonic component of self-inductance, where i is 1, 2, 3.

The values of those parameters are calculated from the FFT analysis of the self-inductance, as shown in Table 5.

Table 5. Amplitude and phase angle of main harmonic components.

Terms	L_{DC} (mH)	L_{m1} (mH)	φ_1 (°)	L_{m2} (mH)	φ_2 (°)	L_{m3} (mH)	φ_3 (°)
Value	2.962	0.102	−2.63	0.063	−75.35	0.030	−2.85

4.2. Mathematical Model in d-q Rotating Coordinate System

In the three-phase static coordinate system, the inductance matrix is time-varying, which would bring about complexity in the process of analysis and control of the machine. The *abc-dq* transformation can transform three AC components into two DC components and one zero-sequence component. It is preferable for vector control strategy.

The conventional *abc-dq* transformation matrix is:

$$P = \frac{2}{3}\begin{bmatrix} \cos(\theta) & \cos(\theta - 120^0) & \cos(\theta + 120^0) \\ -\sin(\theta) & -\sin(\theta - 120^0) & -\sin(\theta + 120^0) \\ \frac{1}{2} & \frac{1}{2} & \frac{1}{2} \end{bmatrix} \tag{19}$$

and:

$$P^{-1} = \begin{bmatrix} \cos(\theta) & -\sin(\theta) & 1 \\ \cos(\theta - 120^0) & -\sin(\theta - 120^0) & 1 \\ \cos(\theta + 120^0) & -\sin(\theta + 120^0) & 1 \end{bmatrix} \tag{20}$$

The no-load flux linkage in the *d-q* rotating coordinate system can be expressed as:

$$\begin{bmatrix} \psi_{md} \\ \psi_{mq} \\ \psi_{m0} \end{bmatrix} = P \begin{bmatrix} \psi_{ma} \\ \psi_{mb} \\ \psi_{mc} \end{bmatrix} = \begin{bmatrix} -\psi_m \\ 0 \\ 0 \end{bmatrix} \tag{21}$$

From Equation (21) it can be observed that ψ_{md} (the value of the *d*-axis component of no-load flux linkage) is equal to the negative value of ψ_m (ψ_m is the fundamental amplitude of the no-load flux linkage). Both ψ_{mq} (value of *q*-axis component of no-load flux linkage) and ψ_{m0} (the value of *0*-axis component of no-load flux linkage) are equal to zero. To verify the aforementioned analysis, the waveforms of ψ_{md}, ψ_{mq} and ψ_{m0} based on the *abc-dq* transformation of FEM results are shown in Figure 11. The average value of ψ_{md}, ψ_{mq} and ψ_{m0} based on the *abc-dq* transformation of 3-D FEM results and the mathematical formula are listed in Table 6. It can be seen that the results from the mathematical formula agree well with the 3-D FEM results, and this verifies the validity of the aforementioned mathematical formula.

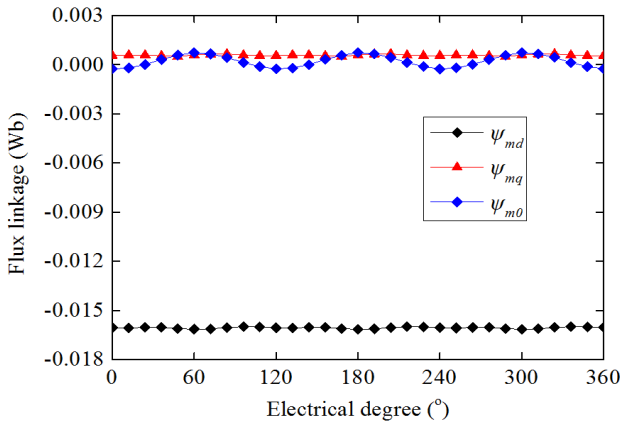

Figure 11. Waveforms of no-load flux linkage in *d-q* rotating coordinate system.

Table 6. No-load flux linkage in *d-q* rotating coordinate system.

Terms	from FEM	from Mathematical Model
ψ_{md} (Wb)	−0.0162	−0.0162
ψ_{mq} (Wb)	0.0006	0
ψ_{m0} (Wb)	0.0002	0

The flux linkage equation after *abc-dq* transformation is written as:

$$\psi' = P\psi = PLi = (PLP^{-1})i' = L'i' \tag{22}$$

Then, the inductance matrix can be written as:

$$\begin{bmatrix} L_d & L_{dq} & L_{d0} \\ L_{qd} & L_q & L_{q0} \\ L_{0d} & L_{0q} & L_0 \end{bmatrix} = L' = PLP^{-1} = P \begin{bmatrix} L_{aa} & L_{ab} & L_{ac} \\ L_{ba} & L_{bb} & L_{bc} \\ L_{ca} & L_{cb} & L_{cc} \end{bmatrix} P^{-1} \tag{23}$$

where $\boldsymbol{\psi}$, $\boldsymbol{L}$ and $\boldsymbol{i}$ is flux linkage matrix, inductance matrix and current matrix in the three-phase static coordinate system, respectively. $\boldsymbol{\psi}'$, $\boldsymbol{L}'$ and $\boldsymbol{i}'$ are flux linkage matrix, inductance matrix and current matrix in the *d-q* rotating coordinate system, respectively.

By substituting the Equations (18)–(20) into (23), the expressions of each components of inductance matrix in the *d-q* rotating coordinate system are written as follows:

$$\begin{aligned} L_d &= L_{DC} + \frac{1}{2}L_{m2}\cos(2\phi_2) + \frac{1}{2}L_{m1}\cos 3(\theta + \frac{\phi_1}{3}) + L_{m3}\cos 3(\theta + \phi_3) \\ L_q &= L_{DC} - \frac{1}{2}L_{m2}\cos(2\phi_2) - \frac{1}{2}L_{m1}\cos 3(\theta + \frac{\phi_1}{3}) + L_{m3}\cos 3(\theta + \phi_3) \\ L_{dq} &= L_{qd} = \frac{1}{2}L_{m2}\sin(2\phi_2) - \frac{1}{2}L_{m1}\sin 3(\theta + \frac{\phi_1}{3}) \\ L_{d0} &= 2L_{0d} = L_{m1}\cos(\phi_1) + L_{m2}\cos 3(\theta + \frac{2\phi_2}{3}) \\ L_{q0} &= 2L_{0q} = L_{m1}\sin(\phi_1) - L_{m2}\sin 3(\theta + \frac{2\phi_2}{3}) \\ L_0 &= L_{DC} + L_{m3}\cos 3(\theta + \phi_3) \end{aligned} \tag{24}$$

From Equation (24) it can be observed that both L_d and L_q are not constant, and they contain three-order harmonic components. L_{dq} is not equal to zero and also contains a three-order harmonic component. This means that the *d*- and *q*- axis are not fully decoupled. The three-order harmonic component contained in the inductance matrix will result in the fluctuation of the thrust force and this will be illustrated in Section 4.3.

The waveforms of three-phase self-inductance are shown in Figure 6a. In Figure 12, the waveforms of L_d´, L_q´, L_0´ and L_{dq}´ are obtained by *abc-dq* transformation of the three-phase self-inductance, and the waveforms of L_d, L_q, L_0 and L_{dq} are obtained by Equation (24), in which the value of variables are listed in Table 5. The average values of the *d*-, *q*- and *0*- axis inductance components based on different methods are listed in Table 7. As we can see, the errors between L_d´, L_q´, L_{dq}´ and L_d, L_q, L_{dq} are very small and their curves are almost the same, which verifies the validity of the aforementioned mathematical formula.

Table 7. Average values of *d*- and *q*- inductance based on different methods.

Terms	L_d	L_d´	L_q	L_q´	L_0	L_0´
Average value (mH)	2.93	2.93	3.00	2.99	2.96	2.96

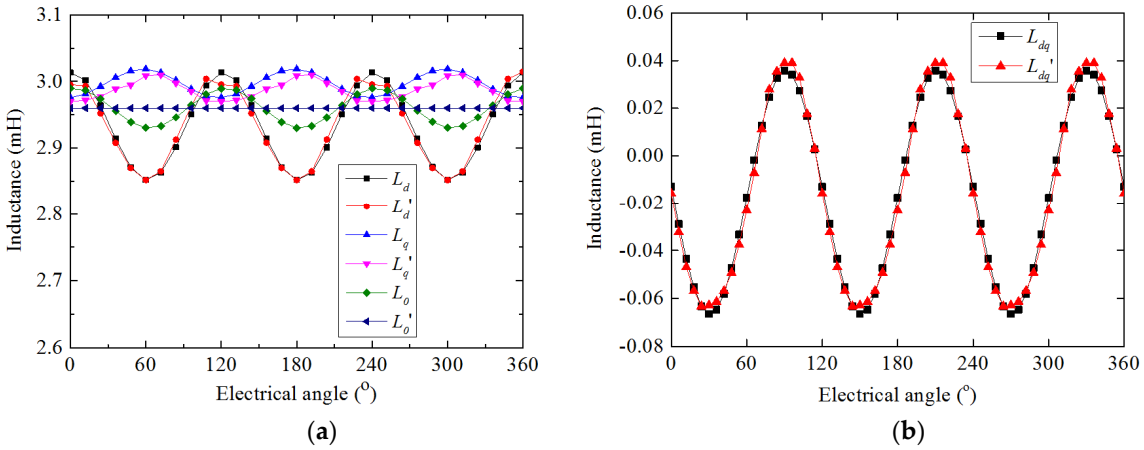

Figure 12. Waveforms of inductances. (**a**) L_d´, L_q´, L_0´ and L_d, L_q, L_0; (**b**) L_{dq}´, L_{dq}.

4.3. Thrust Force in d-q Rotating Coordinate System

The flux linkage equation are written as follows:

$$\begin{aligned} \psi_d &= \psi_{md} + L_d i_d + L_{dq} i_q \\ \psi_q &= L_q i_q + L_{qd} i_d \end{aligned} \tag{25}$$

The voltage equation are written as follows:

$$\begin{aligned} u_d &= \frac{d\psi_d}{dt} - \omega\psi_q + Ri_d \\ u_q &= \frac{d\psi_q}{dt} + \omega\psi_d + Ri_q \end{aligned} \tag{26}$$

On the basis of power conservation, the thrust force of the machine can be derived as:

$$F = \frac{3}{2}\frac{u_d i_d + u_q i_q}{v} \tag{27}$$

By substituting Equations (24)–(26) into (27), and neglecting the stator resistance, the expression of thrust force can be written as:

$$\begin{aligned} F &= \frac{3}{2}\frac{\pi}{\tau}\left\{\psi_{md} i_q + (L_d - L_q) i_d i_q - 3L_{m1}\cos 3(\theta + \frac{\phi_1}{3}) i_d i_q \right. \\ &\left. + [L_{m1}\sin 3(\theta + \frac{\phi_1}{3}) + \frac{1}{2}L_{m2}\sin(2\phi_2)](i_q^2 - i_d^2) - 3L_{m3}\sin 3(\theta + \phi_3)(i_q^2 + i_d^2)\right\} \\ &= F_{PM} + F_r + F_{ar} \end{aligned} \tag{28}$$

where $F_{PM} = \frac{3}{2}\frac{\pi}{\tau}\psi_{md} i_q$ is the PM thrust force, $F_r = \frac{3}{2}\frac{\pi}{\tau}(L_d - L_q) i_d i_q$ is the reluctance thrust force, and $F_{ar} = \frac{3}{2}\frac{\pi}{\tau}\left\{-3L_{m1}\cos 3(\theta + \frac{\phi_1}{3}) i_d i_q + [\frac{1}{2}L_{m2}\sin(2\phi_2) + L_{m1}\sin 3(\theta + \frac{\phi_1}{3})](i_q^2 - i_d^2) - 3L_{m3}\sin 3(\theta + \phi_3)(i_q^2 + i_d^2)\right\}$ is the additional force ripple component.

When $i_d = 0$ control strategy is used, the current matrix in the three-phase static coordinate system can be written as:

$$\begin{bmatrix} i_a \\ i_b \\ i_c \end{bmatrix} = \begin{bmatrix} \sqrt{2} I \sin(\theta) \\ \sqrt{2} I \sin(\theta - 120^0) \\ \sqrt{2} I \sin(\theta + 120^0) \end{bmatrix} \tag{29}$$

Then the current matrix in the *d-q* rotating coordinate system can be written as:

$$\begin{bmatrix} i_d \\ i_q \\ i_0 \end{bmatrix} = P \begin{bmatrix} i_a \\ i_b \\ i_c \end{bmatrix} = \begin{bmatrix} 0 \\ -\sqrt{2}I \\ 0 \end{bmatrix} \tag{30}$$

By substituting Equations (30) into (28), the expression of force can be simplified as:

$$F = \frac{3}{2}\frac{\pi}{\tau}\left\{-\sqrt{2}\psi_{md}I + [2L_{m1}\sin3(\theta + \frac{\phi_1}{3}) + L_{m2}\sin(2\phi_2) - 6L_{m3}\sin3(\theta + \phi_3)]I^2\right\} \tag{31}$$

In order to verify the aforementioned analysis, the waveforms of thrust force based on the proposed mathematical model and 3-D FEM are shown in Figure 13. It can be observed that these two curves also show the same trend and the error between average values is very tiny. Besides, the waveform of thrust force fluctuates three times in one period of alternating current, which is in accordance with Equation (31). The main characteristics of thrust force using the mathematical model and 3-D FEM are listed in Table 8.

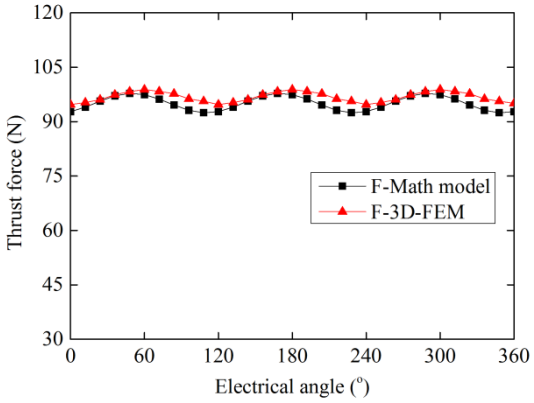

Figure 13. Waveforms of thrust force based on different methods.

Table 8. Characteristic of thrust force based on different methods.

Items	from 3-D FEM	from Mathematical Model
Maximum (N)	98.85	97.80
Minimum (N)	94.72	92.44
Average (N)	96.79	95.12
F_{ripple}	2.14%	2.82%

The comparison of the thrust force results at different load points is shown in Figure 14, with the mathematical model and 3-D FEM. It can be seen from Figure 14a that the error of average value of thrust force calculated through the mathematical model and through 3-D FEM at different load points is very tiny. In Figure 14b, the two curves follow the same trend, which reveals that the peak to-peak value of thrust force increases along with the increase of load. However, the result with the mathematical model is slightly different from that with 3-D FEM. This is mainly because some higher order harmonics components of inductance are neglected in the mathematical model. If all the harmonics components of inductance are considered, the results would be closer. Nevertheless, the comparison results prove the validity and effectiveness of the proposed mathematical model. This provides a powerful foundation for the vector control or direct force control of the STTF-PMLSM.

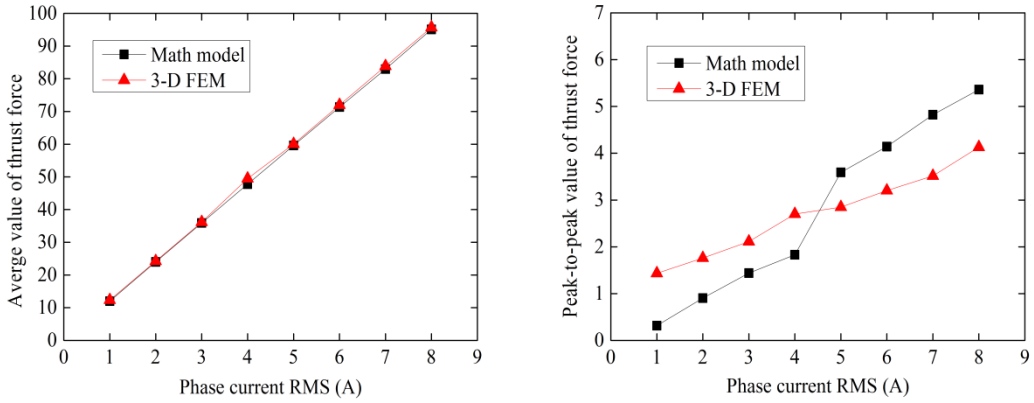

Figure 14. The comparison of results of different methods: (**a**) Average value of thrust force; (**b**) Peak to-peak value of thrust force.

5. Conclusions

The following conclusions can be drawn from the analysis and modeling of the STTF-PMLSM:

(1) The stator core of the STTF-PMLSM is unsegmented and can be fabricated by silicon-iron steel lamination, which can greatly simplify the manufacture process and increase the mechanical strength.

(2) Simplified one phase model can be used to investigate the performance of the machine in order to save the computation time.

(3) The analytical expression of detent force, thrust force, and power factor, has been derived and verified with 3-D FEM, it proves the validity of theoretical analysis.

(4) An improved mathematical model of the STTF-PMLSM based on the *d-q* rotating coordinate system is developed and verified with 3-D FEM, it provide a powerful foundation for the vector control or direct force control of the STTF-PMLSM.

Acknowledgments: This work was supported by National Natural Science Foundation of China under Project 51325701 and 51377033.

Author Contributions: The work presented here was carried out in collaboration between all authors. Shaohong Zhu designed the study and wrote the paper. Bin Yu, Luming Cheng and Weinan Wang edited the manuscript including literature review for feedback from other authors. Ping Zheng supervised the whole thing and provided feedback for improvement from the original manuscript. All authors read and approved the manuscript.

Conflicts of Interest: The authors declare no conflict of interest.

Nomenclature

$\psi_a, \psi_{a0}, \psi_{pm}$	Flux linkage, Wb.
ψ_m	Fundamental amplitude of flux linkage, Wb.
Φ_m	Fundamental amplitude of no-load main magnetic flux, Wb.
Φ_i	Fundamental amplitude of magnetic flux produced by armature current, Wb.
E	Electromotive Force, V.
f	Rated frequency, Hz.
F	Thrust force, N.
F_d	Detent force, N.
F_{em}	Electromagnetic force, N.
I	Current, A.
i	Phase current, A.
j, k, n	Non-negative integer.
L	Winding inductance, mH.
N	Number of turns of the coil.
R	Phase reluctance
R_s	Outer radius of the stator, mm.
τ	Pole pitch, mm.
u	Phase voltage, V.
v	Speed of the linear machine, m/s.
ω	Angular velocity, rad/s.
W'	Magnetic co-energy.
x	Position of the translator, mm.
z	Displacement of the translator, mm.
θ_i	Initial phase angle of the ith harmonic, rad.

References

1. Boldea, I.; Nasar, S.A. *Linear Electric Actuators and Generators*; Cambridge University Press: Cambridge, UK, 2005; pp. 33–43.
2. Shin, J.-S.; Watanabe, R.; Koseki, T.; Kim, H.-J. Transverse flux type cylindrical linear synchronous motor for large thrust using generic armature cores for rotary machinery. *IEEE Trans. Ind. Electron.* **2014**, *61*, 4346–4355. [CrossRef]
3. Wang, J.; Howe, D. Design optimization of radially magnetized, iron cored, tubular permanent-magnet machines and drive systems. *IEEE Trans. Magn.* **2004**, *40*, 3262–3277. [CrossRef]
4. Zhao, M.; Wang, Q.; Zou, J.; Wu, G. Development and analysis of tubular transverse flux machine with permanent-magnet excitation. *IEEE Trans. Ind. Electron.* **2012**, *59*, 2198–2207.
5. Chang, J.-H.; Kang, D.-H.; Lee, J.-Y.; Hong, J.-P. Development of transverse flux linear motor with permanent magnet excitation for direct drive applications. *IEEE Trans. Magn.* **2005**, *41*, 1936–1939. [CrossRef]
6. Kang, D.H.; Chun, Y.H.; Weh, H. Analysis and optimal design of transverse flux linear motor with PM excitation for railway traction. *IEE Proc. Elect. Power Appl.* **2003**, *150*, 493–499. [CrossRef]
7. Zheng, P.; Tong, C.D.; Bai, J.G.; Yu, B.; Sui, Y.; Shi, W. Electromagnetic design and control strategy of an axially magnetized permanent-magnet linear alternator for free-piston stirling engines. *IEEE Trans. Ind. Appl.* **2012**, *48*, 2230–2239. [CrossRef]
8. Wang, J.; West, M.; Howe, D.; La Parra, H.Z.-D.; Arshad, W.M. Design and experimental verification of a linear permanent magnet generator for a free-piston energy converter. *IEEE Trans. Energy Convers.* **2007**, *22*, 299–306. [CrossRef]

9. Wang, J.; Howe, D.; Jewell, G.W. Analysis and design optimization of an improved axially magnetized tubular permanent-magnet machine. *IEEE Trans. Energy Convers.* **2004**, *19*, 289–295. [CrossRef]
10. Wang, J.; Howe, D.; Lin, Z. Design optimization of short-stroke single-phase tubular permanent-magnet motor for refrigeration applications. *IEEE Trans. Ind. Electron.* **2010**, *57*, 327–334. [CrossRef]
11. Clark, R.E.; Smith, D.S.; Mellor, P.H.; Howe, D. Design optimization of moving-magnet actuators for reciprocating electro-mechanical systems. *IEEE Trans. Magn.* **1995**, *31*, 3746–3748. [CrossRef]
12. Weh, H.; May, H. Achievable force densities for permanent magnet excited machines in new configurations. In Proceedings of the International Conference on Electrical Machines, Munchen, Germany, 8–10 Sepember 1986; pp. 1107–1111.
13. Mitcham, A. J. Transverse flux motors for electric propulsion of ships. In Proceedings of IEE Colloquium on New Topologies Permanent Magnet Machines, London, UK, 18 June 1997.
14. Zhu, J.G.; Guo, Y.G.; Lin, Z.W.; Li, Y.J.; Huang, Y.K. Development of PM transverse flux motors with soft magnetic composite cores. *IEEE Trans. Magn.* **2011**, *47*, 4376–4383. [CrossRef]
15. Yang, G.L.; Cheng, D.S.; Zhang, H.; Kou, B.Q. Bidirectional cross-linking transverse flux permanent magnet synchronous motor. *IEEE Trans. Magn.* **2013**, *49*, 1242–1248. [CrossRef]
16. Kang, D. Increasing of thrust force in transverse flux machine by permanent-magnet screen. *IEEE Trans. Magn.* **2005**, *41*, 1952–1955. [CrossRef]
17. Shin, J.-S.; Watanabe, R.; Koseki, T.; Kim, H.-J.; Takada, Y. The design for cogging force reduction of a double-sided transverse flux permanent magnet linear synchronous motor. *IEEE Trans. Magn.* **2014**, *50*, 8205104. [CrossRef]
18. Shin, J.-S.; Watanabe, R.; Koseki, T.; Kim, H.-J. Practical design approach of a transverse flux linear synchronous motor for compact size, small mover weight, high efficiency, and low material cost. *IEEE Trans. Magn.* **2015**, *51*, 8200504.
19. Zheng, P.; Zhu, S.H.; Yu, B.; Cheng, L.M.; Fan, Y.H. Analysis and optimization of a novel tubular staggered-tooth transverse-flux PM linear machine. *IEEE Trans. Magn.* **2015**, *51*, 8111304. [CrossRef]
20. Zheng, P.; Yu, B.; Yan, H.Y.; Sui, Y.; Bai, J.G.; Wang, P.F. Electromagnetic analysis of a novel cylindrical transverse-flux permanent-magnet linear machine. *Appl. Comput. Electromagn. Soc. J.* **2013**, *28*, 879–891.
21. ANSYS Inc. Available online: http://www.ansys.com/Products/Electronics/Electric-Motors (accessed on 12 January 2016).
22. Bianchi, N.; Bolognani, S.; Cappello, A.D.F. Reduction of cogging force in PM linear motors by pole-shifting. *IEE Proc. Elect. Power Appl.* **2005**, *152*, 703–709. [CrossRef]
23. Harris, M.R.; Pajooman, G.H.; Abu Sharkh, S.M. The problem of power factor in VRPM (transverse-flux) machines. In Proceedings of the 1997 Eighth International Conference on (Conference Publication No. 444) Electrical Machines and Drives, Cambridge, UK, 1–3 September 1997; pp. 386–390.